



# Coherent Flow Structures and Pollutant Dispersion in a Street Canyon

Seung-Bu Park<sup>1</sup> · Jong-Jin Baik<sup>2</sup> · Beom-Soon Han<sup>3</sup>

Received: 14 December 2020 / Accepted: 3 September 2021 / Published online: 28 September 2021  
© The Author(s), under exclusive licence to Springer Nature B.V. 2021

## Abstract

Coherent flow structures and pollutant dispersion in a spanwise-long street canyon are investigated using a parallelized large-eddy-simulation model. Low- and high-concentration branches, starting from the downwind top corner and upwind bottom corner, respectively, are detected in the time-averaged field of pollutant concentration, and detailed structures of in-canyon flow and pollutant dispersion following the two branches are demonstrated. When turbulent eddies impinge on the upper downwind wall, low- and high-concentration blobs with U-shaped flow structures appear and move downward. The downdrafts tilt away from the downwind bottom corner and impinge on the canyon bottom, driving horizontally diverging flows. Cellular structures of low-concentration centres and high-concentration edges are induced by the downdrafts and diverging flows. The diverging flows push low-concentration air toward the downwind and upwind building walls, resulting in local divergence and convergence of pollutants on both walls. Time series of pollutant concentration at multiple points illustrate that pollutant concentration at the pedestrian level is highly sensitive to the diverging flows. The multiresolution spectra show that time scales of variations of pollutant concentration and vertical velocity component increase from the canyon top to the pedestrian-level centre, indicating longer time-scale flow structures are dominant inside the street canyon. The multiresolution cospectra also show that the time scale of vertical turbulent transport of pollutants increases from the canyon top to the pedestrian-level centre. At the two bottom corners, however, short and long time-scale transports occur together, confirming that the low-concentration diverging flows transport pollutants downward while short time-scale turbulence transports pollutants upward.

**Keywords** Coherent flow structures · Large-eddy simulation · Pollutant dispersion · Spanwise organized flow · Street canyon

---

✉ Jong-Jin Baik  
jjbaik@snu.ac.kr

<sup>1</sup> School of Environmental Engineering, University of Seoul, Seoul, South Korea

<sup>2</sup> School of Earth and Environmental Sciences, Seoul National University, Seoul, South Korea

<sup>3</sup> Department of Biological and Environmental Engineering, Semyung University, Jecheon, South Korea

## 1 Introduction

As urbanization rapidly progresses globally, controlling air quality in urban areas has attracted more and more interest. Along with air quality issues, wind environments of various horizontal urban scales have also gained much interest. Among the various urban scales, the local urban scale less than 100–200 m, the so-called microscale or street scale (Britter and Hanna 2003), is the scale of airflow and pollutant dispersion mostly affecting traffic-related pollutants at the pedestrian level, where people are directly exposed. Thus, we need to understand and accurately predict microscale flow and pollutant dispersion in urban areas to prevent potential adverse health problems (Marshall et al. 2009). Microscale urban flow and pollutant dispersion, however, are very complicated because of mechanically and thermally generated turbulence over the complex layout of urban buildings and mesoscale and synoptic-scale meteorological factors (Park et al. 2015).

To rule out the complexities and understand the fundamental characteristics of microscale urban flow and pollutant dispersion, flow and pollutant dispersion in a street canyon, on-road space flanked by buildings on both sides, have been investigated for several decades through wind-tunnel experiments, field observations, and numerical simulations (Sini et al. 1996; Baik and Kim 1999; Caton et al. 2003; Letzel et al. 2008; Xie and Castro 2009; Park et al. 2012; Zhong et al. 2015; Kwak et al. 2016; Duan et al. 2019). The air in a street canyon can be isolated or open to the outer environment depending on the ambient wind direction and the ratio of building height to road width (Oke 1988). Because the street canyon is a very basic unit of urban morphology and it can represent both isolated and open urban environments, it has also been used as a framework to parametrize urban physical processes in numerical weather and climate models (Oleson et al. 2008; Ryu et al. 2011). When the ambient flow is in the parallel and slantwise directions to the street canyon, channelling and helical flows appear, respectively, and in-canyon air is mixed with the overlying atmosphere to some extent (Belcher 2005; Xie and Castro 2009). On the contrary, when the ambient flow is perpendicular to the direction of the street canyon, a primary vortex (or a cross-canyon vortex) appears and in-canyon air can be isolated from the overlying atmosphere with traffic-related pollutants being trapped in the street canyon (Oke et al. 2017).

Along with the magnitude of pollutant emission in a street canyon, the exchange of in-canyon air and overlying ambient air across the canyon top is crucial for determining the in-canyon pollutant concentration. Baik and Kim (2002) showed that pollutants between a street canyon and the overlying ambient air are mainly transported by turbulent diffusion processes based on their Reynolds-averaged Navier–Stokes (RANS) equation model simulation. Turbulent eddies responsible for the turbulent diffusion processes have been visualized by using particle image velocimetry (Caton et al. 2003) and by large-eddy simulation (LES) (Walton and Cheng 2002). A cavity shear layer develops at the canyon top and fluctuations of the interfacial shear layer induce intermittent puffs of pollutants at the canyon top, with a characteristic time scale of 30–60 s, and the escaped puffs move downstream following the ambient flow (Walton and Cheng 2002). The fluctuations of the cavity shear layer and the ejection of pollutants are dependent on the incoming turbulence intensity, and the removal of in-canyon pollutants is affected by the size of coherent structures such as low-speed streaks (Michioka and Sato 2012).

Although pollutant dispersion occurring across the canyon top has been studied extensively, pollutant dispersion within the street canyon has not been sufficiently investigated yet. Recently, Duan et al. (2019) revealed that the pattern of pollutant dispersion can be significantly different depending on the position of the pollution source and other conditions.

However, the kinematics of turbulent eddies and scalars inside the street canyon have not been sufficiently demonstrated in the previous studies: for example, how incoming turbulent eddies and incoming perturbations of pollutants proceed inside the street canyon and how they interact with the primary and corner vortices. Incoming eddies are one of the important factors that affect pedestrian-level air quality, but their role is not completely understood. While the spanwise structure of external coherent structures has been investigated (Michioka and Sato 2012; Park et al. 2013), the spanwise structure of in-canyon turbulent eddies is not investigated yet to the authors' knowledge. It would be of interest to study how the turbulent eddies impinging on the canyon bottom affect pollutant dispersion, especially at the pedestrian level.

Our study investigates the role of coherent flow structures in the pollutant dispersion in a street canyon. We perform high-resolution numerical simulation of street-canyon flow and pollutant dispersion and illustrate their coherent structures, especially in the pedestrian-level and near-wall regions. The numerical model and simulation set-up are described in Sect. 2. The simulation results are presented and discussed in Sect. 3. A summary and conclusions are given in Sect. 4.

## 2 Numerical Model and Simulation Set-Up

We use the parallelized LES model (PALM) version 6.0 (Maronga et al. 2020), which solves the implicitly filtered Navier–Stokes equations in Boussinesq-approximated form. The prognostic variables are the velocity components  $u$ ,  $v$ ,  $w$ ; passive scalar concentration  $s$ ; and subfilter-scale turbulence kinetic energy (TKE) on a staggered Arakawa C-grid (Arakawa and Lamb 1977). The velocity components  $u$ ,  $v$ , and  $w$  are in the streamwise ( $x$ ), spanwise ( $y$ ), and vertical ( $z$ ) directions, respectively. A third-order Runge–Kutta scheme (Williamson 1980) is used for time integration, and advection terms are discretized using an upwind-biased 5th-order scheme (Wicker and Skamarock 2002). Because PALM is based on the implicitly filtered equations, the filter size is equal to the grid size, and subgrid-scale (SGS) eddies are parametrized based on inertial subrange theory. The SGS fluxes of momentum and scalars are parametrized using the 1.5-order Deardorff scheme (Deardorff 1980) in which eddy viscosity and eddy diffusivity are calculated using the SGS TKE. If the grid size is appropriately set (e.g., smaller than the size of eddies of interest), energy-containing turbulent eddies can be quite accurately simulated using affordable computing resources. Therefore, PALM has been widely used in studying urban flow and pollutant dispersion, planetary boundary layers, and (cloudy) convective circulations (Maronga et al. 2015). Along with its wide applications, it has also been validated many times against field measurements and wind-tunnel experiments (Letzel et al. 2008; Maronga et al. 2013; Yaghoobian et al. 2014; Han et al. 2018). Flow and pollutant dispersion in this kind of long street canyon have also been validated. For example, Park et al. (2012) validated simulations of the normalized streamwise velocity component in a street canyon by comparing these with the wind-tunnel measurements of Uehara et al. (2000), while Han et al. (2018) compared PALM-simulated scalar concentrations with the wind-tunnel measurements of Pavageau and Schatzmann (1999), showing a good agreement between the simulation and the measurements.

A simple urban topography, in which 20-m wide, 20-m ( $H$ ) high, and 160-m long buildings are evenly spaced at 20 m apart, is considered (Fig. 1). While a doubly periodic boundary condition is implemented at the horizontal boundaries for the velocity components and SGS TKE, Dirichlet and Neumann conditions for the pollutant concentration are implemented,

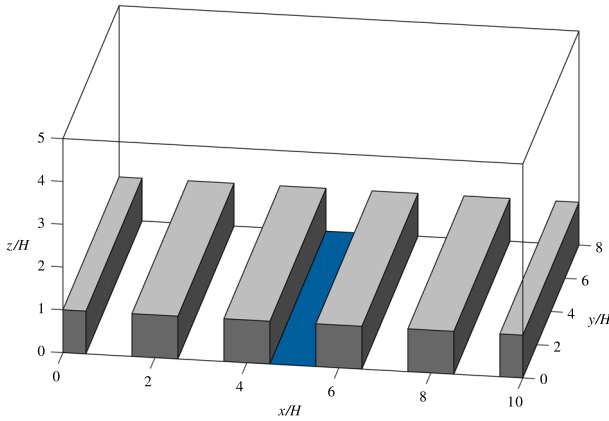


**Fig. 1** Computational domain and building configuration. Pollutants are emitted from the blue shaded area. Here,  $H$  is the building height

respectively, at the inflow ( $x/H = 0$ ) and outflow ( $x/H = 10$ ) boundaries with a periodic boundary condition in the  $y$  direction. Thus, this urban topography represents long canyons being repeated in the  $x$  direction, and non-polluted air comes into the domain continuously. The grid size in the  $x$  and  $y$  directions is 0.3125 m, and the grid size in the  $z$  direction is 0.3125 m below  $z = 50$  m and gradually stretched to 1 m above that level. The computation domain with  $640 \times 512 \times 216$  grid boxes covers  $200 \times 160 \times 101.5 \text{ m}^3$ , and 64 grid boxes per canyon width (or per canyon height) resolve in-canyon turbulent eddies, satisfying the criteria of spatial resolution suggested by Xie and Castro (2006). Neutrally buoyant unitless pollutants are emitted from the bottom surface of the central street canyon ( $4.5 \leq x/H \leq 5.5$ ,  $0 \leq y/H \leq 8$ ), and its emission flux is  $10 \text{ m s}^{-1}$ . The unitless pollutant can be regarded as a gaseous pollutant such as carbon monoxide, and then the emission flux would be equivalent to  $10 \text{ ppm m s}^{-1}$  ( $\approx 11.456 \text{ mg m}^{-2} \text{ s}^{-1}$ ). The Coriolis force is ignored, and the flow is driven by a constant external pressure gradient in the  $x$  direction ( $-0.0004 \text{ Pa m}^{-1}$ ) instead of specifying the geostrophic wind. A quasi-steady state is maintained by the constant external pressure gradient, and the freestream velocity, for example, horizontally-averaged streamwise velocity component at  $z = 5H$  ranges from  $3.2$  to  $3.6 \text{ m s}^{-1}$ . The timestep is dynamically determined to satisfy the Courant–Friedrichs–Lewy condition, and it ranges from 0.061 to 0.082 s. A constant flux layer between the solid surfaces and the grid points closest to the solid surfaces is assumed, and Monin–Obukhov similarity theory is used to calculate the surface momentum and scalar fluxes. The roughness length for both momentum and scalar is 0.01 m. Numerical integrations are performed for 1 h, and the simulation results for the last 30 min are used for analysis.

### 3 Results and Discussion

#### 3.1 Turbulent Flow and Pollutant Dispersion

Figure 2 shows the fields of time-averaged streamlines, spanwise vorticity ( $\partial \bar{u} / \partial z - \partial \bar{w} / \partial x$ ), and pollutant concentration around the central street canyon, the axis of which is located at  $(x/H, z/H) = (5, 0.5)$ . Here, overbars indicate time-averages for 1800 s. The streamlines

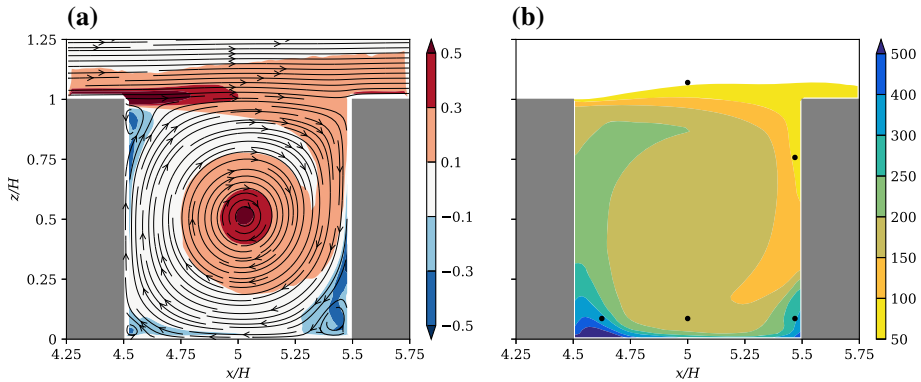


**Fig. 2** Fields of **a** streamlines and vorticity ( $\text{s}^{-1}$ ), calculated from the time-averaged  $u$  and  $w$  components, and **b** time-averaged pollutant concentration at  $y/H = 1.99$ . The black dots in **b** represent the five points where time series of  $u$ ,  $w$ , and  $s$  are analyzed in Sect. 3.2

and vorticity fields illustrate that a primary vortex exists in the street canyon and three small counter-rotating vortices exist at three canyon corners (the top and bottom corners near the upwind building wall and the bottom corner near the downwind building wall), as reported by Letzel et al. (2008), Park et al. (2012), and Duan et al. (2019). While the two bottom corner vortices were observed in the simulation results of a two-dimensional RANS model by Baik and Kim (2002), the top corner vortex was not simulated by the RANS model and it was not observed even in the three-dimensional LES model results (Cui et al. 2004). The simulation of the corner vortices seems to be sensitive to the parametrization of SGS eddies, especially near the walls. The time-averaged pollutant concentration field illustrates that pollutant dispersion generally follows the mean circulation in the street canyon. There are two main concentration branches following the primary canyon vortex: a low-concentration branch incoming from above the street canyon and a high-concentration branch rising from the upwind bottom corner. Interestingly, the two branches seem to be separated from each other even in this time-averaged pollutant concentration field as shown by the wind-tunnel experiment of Pavageau and Schatzmann (1999). Below  $z/H \approx 0.25$ , the low-concentration branch tilts away from the downwind bottom corner vortex, and a portion of bottom-emitted pollutants is trapped in the corner vortex. The high-concentration branch also tilts away from the upwind top corner vortex. It is notable that the high-concentration rising branch does not directly cross the canyon top, implying that a small portion of pollutants escapes the street canyon following ejecting turbulent eddies and the rest of pollutants just circulate within the street canyon.

To demonstrate instantaneous features of pollutant dispersion, snapshots of pollutant concentration at multiple time instants are presented in Fig. 3. At  $t = 3534$  s, one relatively large low-concentration blob is passing by the centre of the canyon top, and the blob moves downstream to the downwind wall and then downward to the upper boundary of the region where the downwind corner vortex dominates (Fig. 3b–e). The low-concentration blob structure tilts away from the downwind bottom corner while breaking into smaller structures, which are swept to the upwind bottom corner (Fig. 3f–h). Afterwards, the low-concentration blobs rise following the primary vortex to the upper central part of the street canyon (Fig. 3i–l). Note that they pass the region below the centre of the canyon top where the high-concentration branch ends (Fig. 2b). Another low-concentration blob at  $t = 3534$  s and centred at  $(x/H,$

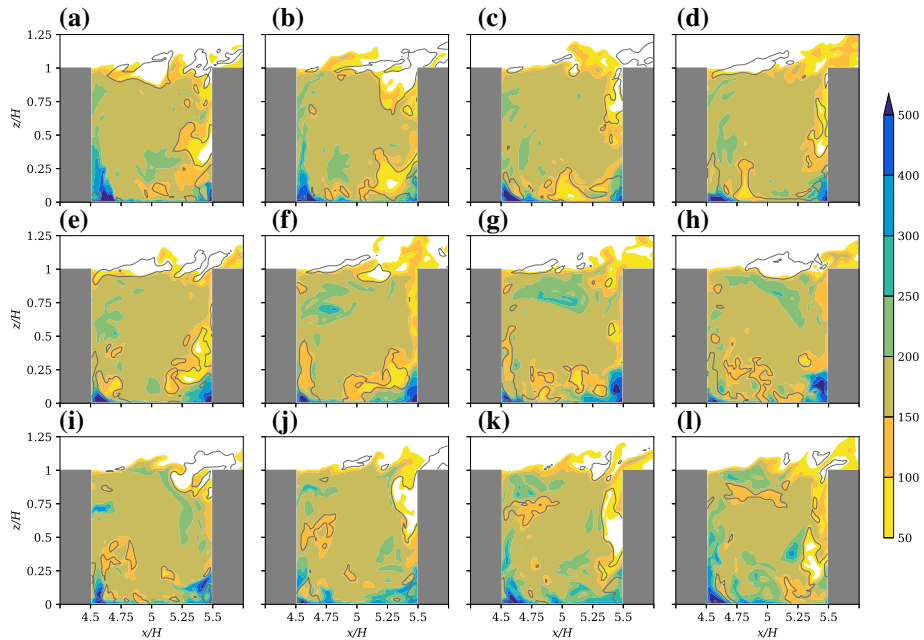


**Fig. 3** Instantaneous fields of pollutant concentration at  $y/H = 1.99$  and at **a**  $t = 3534$  s, **b**  $t = 3540$  s, **c**  $t = 3546$  s, **d**  $t = 3552$  s, **e**  $t = 3558$  s, **f**  $t = 3564$  s, **g**  $t = 3570$  s, **h**  $t = 3576$  s, **i**  $t = 3582$  s, **j**  $t = 3588$  s, **k**  $t = 3594$  s, and **l**  $t = 3600$  s. Grey contours show concentration perturbations (deviation from time-averaged concentration) of  $-35$

$y/H, z/H) \approx (5.43, 1.99, 0.35)$  circulates and pushes the air around the upwind bottom corner. Then, high-concentration structures [e.g., a high-concentration blob at  $t = 3552$  s and centred at  $(x/H, y/H, z/H) \approx (4.65, 1.99, 0.42)$ ] rise to the upper central part of the street canyon and then sink toward the downwind wall following the primary vortex (Fig. 3d–h). Based on the series of snapshots, it takes one minute or a little longer for an external eddy to circulate the street canyon unless it is not broken on the way. This kind of eddy circulation is repeated all through the simulation (not shown).

More details of the turbulent eddies impinging on the downwind wall and the consequent dispersion of fresh and polluted air are presented in Fig. 4. The contours of the streamwise velocity component ( $-0.13 \text{ m s}^{-1}$ ) display many U-shaped flow structures being expelled from the downwind wall, and they are actually the boundaries between newly impinged eddies and stagnant or slowly moving eddies near the downwind wall. The value of  $-0.13 \text{ m s}^{-1}$  is manually selected to visualize the U-shaped flow structures optimally, and the visualization of U-shaped flow structures is possible all through the 30-min analysis period (not shown). The U-shaped flow structures move downward and low-concentration and high-concentration (e.g.,  $s > 150$ ) blobs follow them, as shown in the snapshots of Fig. 3. It is notable that not only low-concentration blobs but high-concentration blobs appear near the upper downwind wall, confirming that a portion of bottom-emitted pollutants are trapped and circulate toward the downwind wall. Below  $z/H \approx 0.3$ , where the counter-rotating corner vortex dominates, high-concentration structures appear side by side and the spacing between two high-concentration structures is  $\approx 0.4\text{--}0.5H$ . Between the two high-concentration structures, turbulent eddies elongated in the spanwise direction appear, for example, at  $t = 3600$  s and centred at  $(x/H,$

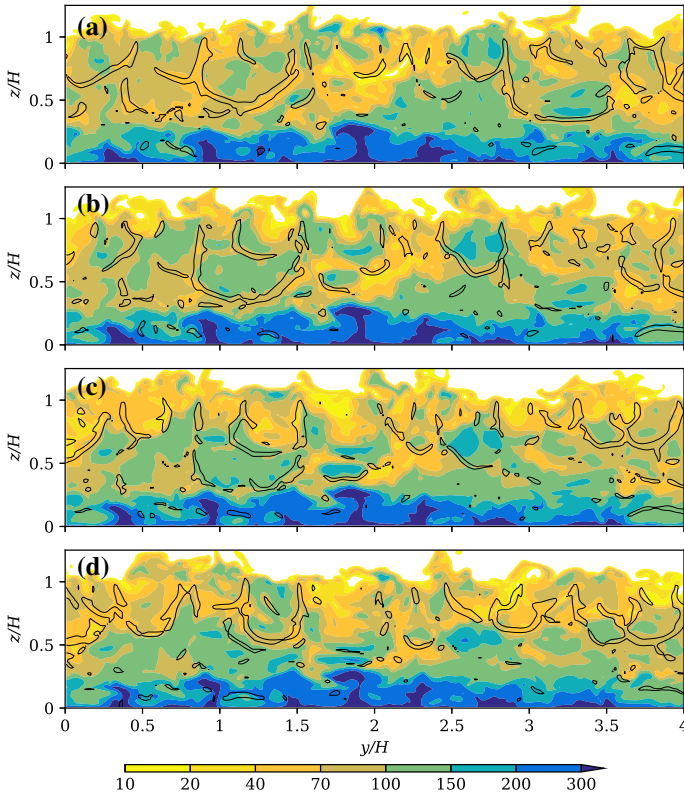


**Fig. 4** Instantaneous fields of pollutant concentration at  $x/H = 5.48$  and at **a**  $t = 3591$  s, **b**  $t = 3594$  s, **c**  $t = 3597$  s, and **d**  $t = 3600$  s. Black contours show the streamwise velocity component of  $-0.13 \text{ m s}^{-1}$

$y/H, z/H \approx (5.48, 1.15, 0.10)$ . These eddies, being expelled from the lower downwind wall, indicate that flows toward the lower downwind wall exist between the high-concentration structures.

Near the ground of the street canyon, cellular structures of low-concentration centres and higher-concentration edges appear (Fig. 5). The low-concentration centres are generated by the downdrafts, impinging on the ground, and they expand horizontally with time. The horizontally expanding eddies collide with each other and narrow weak updrafts, indicated by contours of the vertical velocity component of  $0.08 \text{ m s}^{-1}$  in Fig. 5, are generated at the colliding boundaries where the higher-concentration edges appear. This generation mechanism of low- and higher-concentration structures is similar to the generation mechanism of cold pools from moist convective systems (Gentine et al. 2016), with the exception that the downwind wall instead of rain evaporation generates the driving downdrafts. As new downdrafts impinge on the bottom surface successively, low- and higher-concentration structures are generated repeatedly and they move toward the upwind wall, being forced by the primary vortex. The advection of higher-concentration edges and the upwind bottom corner vortex make bottom-emitted pollutants converge at the upwind bottom corner of the street canyon. The downdrafts, impinging on the bottom surface, also induce diverging flows toward the downwind wall, and the diverging flows impinge on the downwind wall. As multiple diverging flows impinge on the downwind wall, low-concentration regions appear side by side



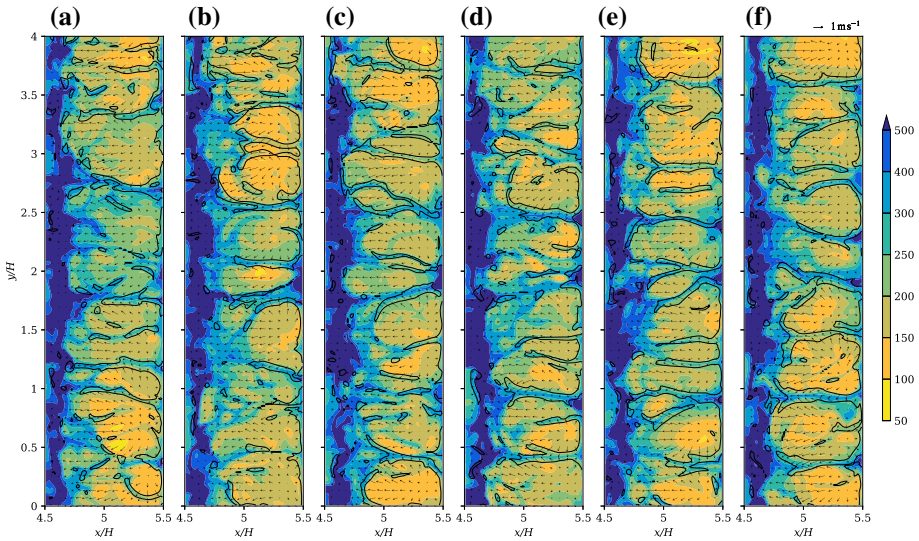


**Fig. 5** Instantaneous fields of pollutant concentration at  $z/H = 0.02$  and at **a**  $t = 3534$  s, **b**  $t = 3546$  s, **c**  $t = 3558$  s, **d**  $t = 3570$  s, **e**  $t = 3582$  s, and **f**  $t = 3594$  s. Black contours show the vertical velocity component of  $0.08 \text{ m s}^{-1}$

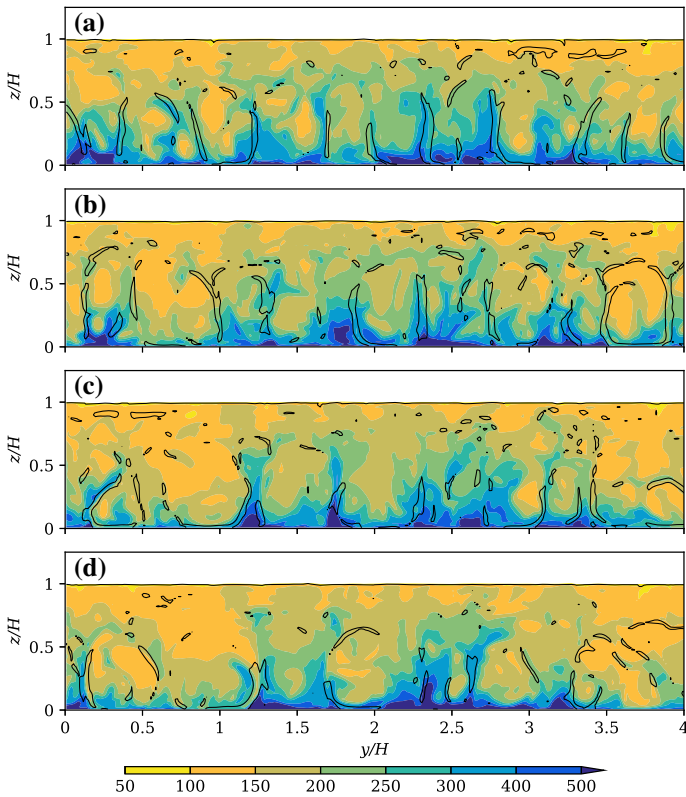
near the lower downwind wall and bottom-emitted pollutants are pushed out into the regions between the low-concentration regions (Fig. 4).

Figure 6 presents the instantaneous fields of pollutant concentration near the upwind wall. The horizontally expanding eddies with low-concentration air move to the upwind wall, and they generate circular low-concentration blobs near the surface of the upwind wall. The turbulent eddies, being impinged on the upwind wall, collide with each other and vertically elongated flow structures are generated between the impinged eddies as visualized by contours of the streamwise velocity component of  $0.1 \text{ m s}^{-1}$  in Fig. 6. The bottom-emitted pollutants converge on the regions between the impinged eddies and they appear as high-concentration vertical plumes shown in Figs. 2 and 3. It is also notable that the spacing between the impinged eddies is similar to that in Fig. 4 ( $\approx 0.4\text{--}0.5H$ ).

### 3.2 Time Series and Multiresolution Spectra

Time series of  $u$ ,  $w$ , and  $s$  are analyzed to show the impacts of the in-canyon flow structures on instantaneous pollutant concentration (Fig. 7). We select five points representing the canyon-top shear layer, the impingement region near the upper downwind wall, the bottom centre, the downwind bottom corner, and the upwind bottom corner, respectively (Fig. 2b). The last three points are at  $z = 1.72 \text{ m}$  ( $z/H = 0.09$ ) to demonstrate the atmospheric environment at the pedestrian level. Note that the two bottom corner points at  $x/H = 4.63$  and  $5.47$  are not symmetric with respect to the canyon centre ( $x/H = 5$ ). The two points are intentionally moved to the asymmetric positions because the roles of horizontally diverging flows and local updrafts can be highlighted together at the two positions. In the canyon-top shear layer, intermittent peaks of pollutant concentration appear with short time-scale updrafts, but not all updrafts accompany high-concentration events. The events of faster downdrafts (high  $u$  and low  $w$ , e.g., at  $t = 3410\text{--}3425$  s), so-called sweep events, induce low-concentration events.





**Fig. 6** Instantaneous fields of pollutant concentration at  $x/H = 4.52$  and at **a**  $t = 3534$  s, **b**  $t = 3546$  s, **c**  $t = 3558$  s, and **d**  $t = 3570$  s. Black contours show the streamwise velocity component of  $0.1 \text{ m s}^{-1}$

At the impingement point in front of the upper downwind wall, strong downdrafts occur with low-concentration events (Fig. 7b). The time scale of downdrafts seems to be longer than that in the canyon-top shear layer. The time scale of pollutant concentration variation at the impingement point also tends to be longer than that in the canyon-top shear layer. Longer time-scale undulation of the three variables  $u$ ,  $w$ , and  $s$  is observed at the pedestrian level right above the bottom centre (Fig. 7c), and this undulation is relevant to the vertical structure of turbulence in a street canyon (Rotach 1995; Eliasson et al. 2006). Along with the undulation, local updrafts with high-concentration events occur (e.g., at  $t \approx 3570$  s) and they are related to the high-concentration edges shown in Fig. 5. At the downwind bottom corner, the pollutant concentration tends to be inversely proportional to the streamwise velocity component because diverging flows toward the downwind wall push low-concentration air to the lower downwind wall (Fig. 7d). Another feature is that short time-scale fluctuations weaken in the downwind bottom corner, and this corresponds to the fact that the energy cascade and turbulence are suppressed within vortices (McWilliams 1990). Short time-scale fluctuations also weaken in the upwind bottom corner, and the pollutant concentration is highly correlated to the streamwise velocity component there (Fig. 7e). This indicates that the diverging flows originating from the strong downdrafts bring low-concentration air toward the upwind wall (Fig. 3).

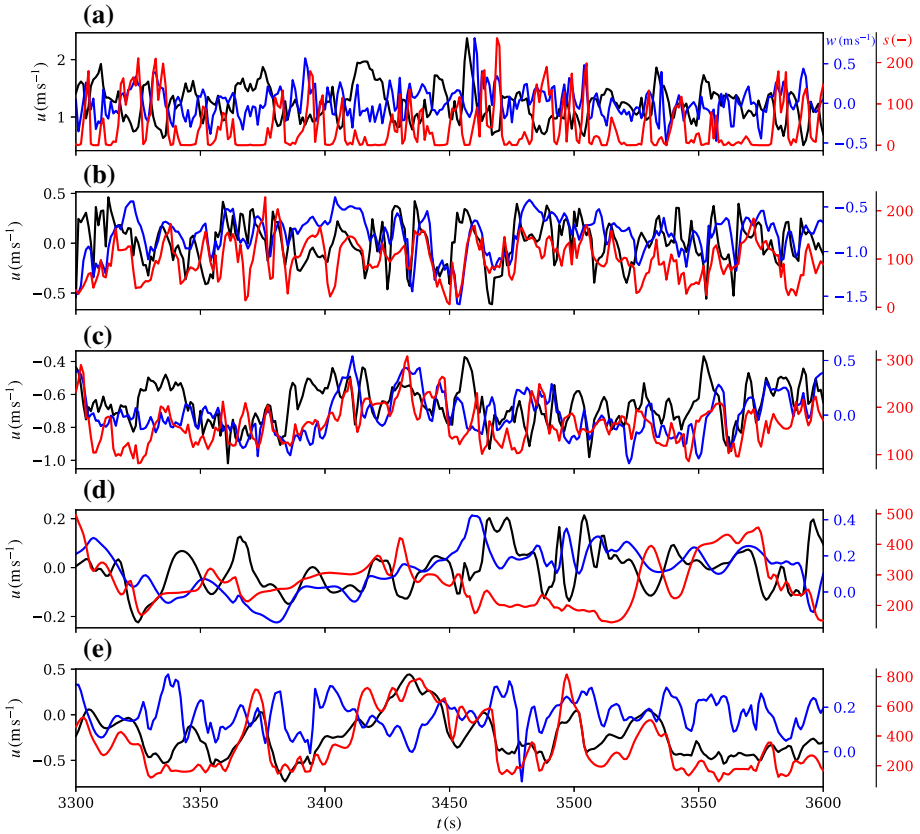


**Fig. 7** Time series of the streamwise (black) and vertical (blue) velocity components, and pollutant concentration (red) at  $(x/H, y/H, z/H)$  = **a** (5, 1.99, 1.07), **b** (5.47, 1.99, 0.76), **c** (5, 1.99, 0.09), **d** (5.47, 1.99, 0.09), and **e** (4.63, 1.99, 0.09)

The multiresolution spectra and cospectra are calculated using the multiresolution decomposition method (Howell and Mahrt 1997; Vickers and Mahrt 2003). For a given series  $w_i$  of  $2^M$  points, segment averages and residual series are successively calculated from the  $2^M$  to the  $2^1$  averaging scales and those at the  $2^m$ -point averaging scale ( $m$ th averaging scale) are as follows (Vickers and Mahrt 2003)

$$\bar{w}_n(m) = \frac{1}{2^m} \sum_{i=I}^J wr_i(m), \tag{1}$$

$$wr_i(m) = wr_i(m + 1) - \bar{w}_n(m + 1). \tag{2}$$

In Eq. 1, the segment number  $n$  is  $1, \dots, 2^{M-m}$ , and the first index  $I$  and the last index  $J$  in each segment are  $(n - 1)2^m + 1$  and  $n2^m$ , respectively. First, the average of all the  $2^M$  points [ $\bar{w}_1(M)$ ] and the residual series [ $wr_i(M - 1)$ ] are calculated where  $wr_i(M)$  is equal to the original series  $w_i$ . Then, two segment averages of the residual series [ $\bar{w}_1(M - 1), \bar{w}_2(M - 1)$ ], each having  $2^{M-1}$  points, and a new residual series from the new segment averages are calculated. This step is repeated until the width of the segment (the averaging scale) becomes  $2^1$ . After that, the residual series  $wr_i(0)$  at the  $2^0$ -point averaging scale is calculated and

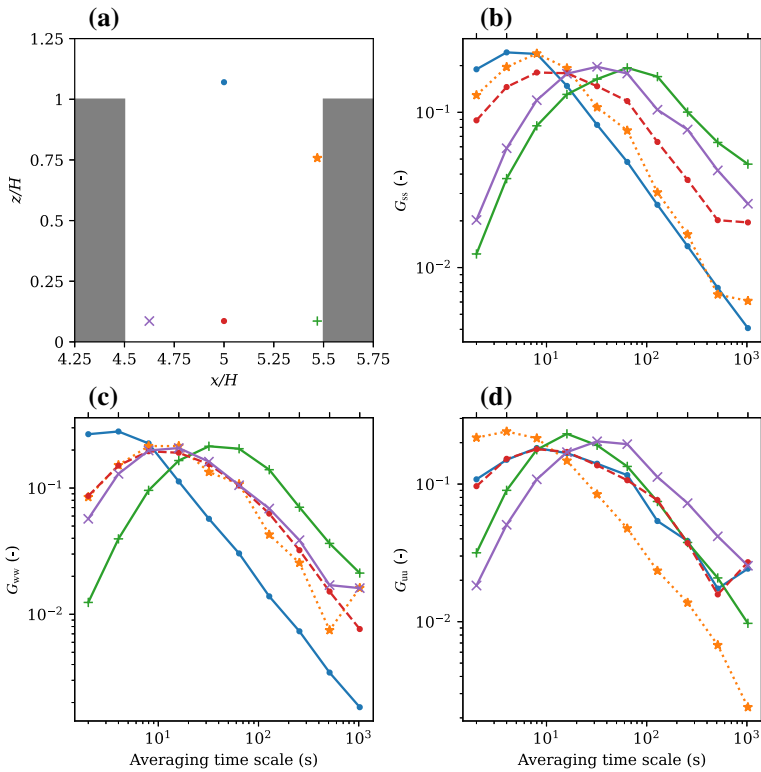


**Fig. 8** **a** Illustration of five positions at which multiresolution spectra are calculated. Multiresolution spectra of **b** pollutant concentration, **c** vertical velocity component, and **d** streamwise velocity component at the five positions. The spectra are normalized by local variances and averaged in the spanwise direction

the residual series is equal to the segment averages at the same scale ( $m = 0$ ). The second moments of the segment averages are the multiresolution spectra, and the spectra at  $2^m$ -point averaging scale are

$$D_{ww}(m) = \frac{1}{2^{M-m+1}} \sum_{n=1}^{2^{M-m+1}} \bar{w}_n^2(m-1). \tag{3}$$

In a similar way, the multiresolution cospectra are obtained by calculating segment averages and residual series of two variables. For example, the multiresolution cospectra of  $w_i$  and  $s_i$  at  $2^m$ -point averaging scale are

$$D_{ws}(m) = \frac{1}{2^{M-m+1}} \sum_{n=1}^{2^{M-m+1}} \bar{w}_n(m-1) \bar{s}_n(m-1). \tag{4}$$

Normalized multiresolution spectra of  $w_i$  and normalized cospectra of  $w_i$  and  $s_i$  are given by

$$G_{ww}(m) = \frac{D_{ww}(m)}{\sum |D_{ww}|}, \quad (5)$$

$$G_{ws}(m) = \frac{D_{ws}(m)}{\sum |D_{ws}|}. \quad (6)$$

In contrast to the Fourier decomposition, the multiresolution decomposition does not use global basis functions and thus it can be implemented in non-periodic series such as the time series in Fig. 7. Additionally, the fast Haar transform algorithm used in the multiresolution decomposition enables faster calculations than the fast Fourier transform (Howell and Mahrt 1997). We calculate the multiresolution spectra and cospectra for the last  $2^{10}$  s at  $y/H = 0-8$  and at the five positions (shown in Fig. 2b). At each  $x-z$  position, 512 multiresolution spectra and cospectra are calculated, and normalized and spanwise-averaged spectra and cospectra are presented in Figs. 8 and 9, respectively.

The multiresolution spectra of pollutant concentration (Fig. 8b) show that the spectrum at the downwind bottom corner has a peak at the 64-s averaging time scale and a spectral peak occurs at the 32-s averaging time scale at the other bottom corner near the upwind wall. At the other three positions, the spectral peaks occur at the 4 to 8-s averaging time scales. This indicates that flow structures around the two bottom corners induce longer time-scale variations of pollutants. The spatial variation of peak averaging time scale is also prominent in the multiresolution spectra of the vertical velocity component (Fig. 8c). From the shear-layer position to near the bottom centre, the peak amplitude of the non-normalized  $w$  spectra decreases (not shown) and the peak averaging time scale increases from 4 to 8 s. At the downwind bottom corner, the peak averaging time scale further increases to 32 s. It is interesting that the multiresolution spectra at the upper downwind wall, bottom centre, and upwind bottom corner positions collapse onto a single curve. We suspect that this is attributed to the connection of U-shaped eddies at the upper downwind wall and downdrafts and diverging flows at the canyon bottom. The normalized multiresolution spectrum of the streamwise velocity component has a 8-s peak at the shear-layer position and a 4-s peak at the upper downwind wall position, indicating that the dominant time scale of  $u$  perturbations becomes shorter after impinging on the downwind wall. At the three pedestrian-level positions, the spectral peak occurs at the 8 to 32-s averaging time scales, longer than the 4-s averaging time scale at the upper downwind wall position. It seems that the  $w$  spectra at the shear-layer position and the  $u$  spectra at the upper downwind wall position do not reveal an inertial subrange, but this is attributed to the coarse sampling frequency (1 s) not to the multiresolution decomposition method.

The different time-scale turbulent eddies also affect the streamwise and vertical turbulent transport of pollutants. The multiresolution cospectra of  $w$  and  $s$  in Fig. 9a illustrate how turbulent eddies of multiple time scales transport pollutants in the vertical direction. In the canyon-top shear layer, pollutants are mostly transported by short time-scale eddies and thus a spectral peak occurs at the 8-s averaging time scale. The peak averaging time scale increases from the shear-layer position to the upper downwind wall position and to the bottom centre position. At the two bottom corner positions, however, the cospectra are positive and negative at short and long averaging time scales, respectively. This means that long time-scale in-canyon circulations transport low-concentration air upward (negative flux) while short time-scale turbulent eddies transport high-concentration air upward (positive flux). Note that the cospectra become positive at all the averaging time scales when we select another pedestrian-level position very close to the upwind wall (e.g.,  $x/H = 4.53$ ) because wall-induced turbulent eddies are more influential than the in-canyon circulations there (not shown). The multiresolution cospectra of  $u$  and  $s$  in Fig. 9b illustrate another interesting fea-

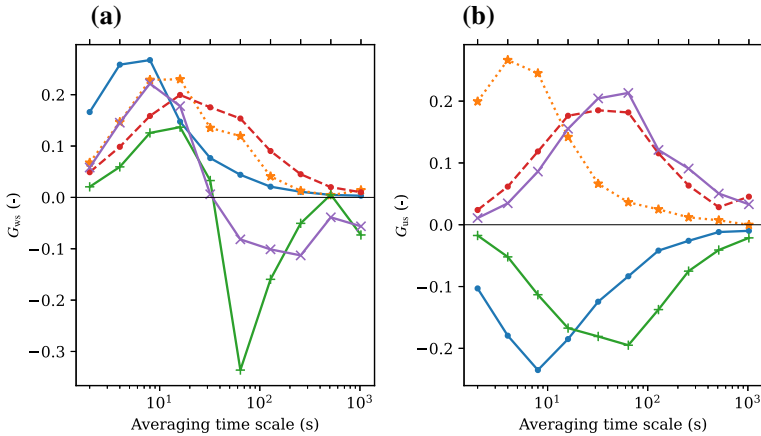


**Fig. 9** Multiresolution cospectra of **a** the vertical velocity component and pollutant concentration and **b** the streamwise velocity component and pollutant concentration at the five positions marked in Fig. 8a. The cospectra are normalized by local total fluxes and averaged in the spanwise direction

ture of pollutant transport. While short time-scale turbulence in the canyon-top shear layer induces negative transport of pollutants (flux toward upstream), longer time-scale circulations, with a peak at the 64-s averaging time scale, induce positive transport of pollutants at the bottom centre and upwind bottom corner positions. At the other bottom corner position, negative transport occurs and its spectral peak occurs at the 64-s averaging time scale. The positive and negative streamwise transports of pollutants around the two bottom corners seem to be accompanied by the low-concentration airs being pushed toward the upwind wall and toward the downwind wall, respectively, but this needs a further in-depth investigation.

## 4 Summary and Conclusions

Coherent flow structures and pollutant dispersion in a street canyon were investigated using an LES model. Low- and high-concentration branches, coming through the downwind top corner and rising from the upwind bottom corner, respectively, are found in the time-averaged pollutant concentration field. Instantaneous features of turbulent eddies and pollutant dispersion following the two branches are illustrated. When turbulent eddies impinge on the upper downwind wall, low- and high-concentration blobs appear with U-shaped flow structures and the turbulent eddies and blobs move downward, following the downwind wall. The downward-moving eddies tilt away from the downwind bottom corner and they impinge on the canyon bottom, inducing horizontally diverging flows. Then, the diverging flows induce cellular structures composed of low-concentration centres and high-concentration edges. A portion of the low-concentration air is transported toward the downwind wall by the diverging flows, and the diverging flows and the primary vortex flow transport another portion toward the upwind wall. This results in local divergence and convergence of pollutants on the downwind and upwind walls, and the converged high-concentration air on the upwind wall rises to the upper central part of the street canyon. This highlights the fact that various coherent flow structures are connected to each other and their combination drives the transport of pollutants.

The time series of pollutant concentration at the five points demonstrate that pedestrian-level pollutant concentration heavily depends on the horizontally diverging flows. The spanwise-averaged multiresolution spectra illustrate that the time scale of pollutant concentration variation increases from the canyon-top shear layer into the street canyon because longer time-scale flow structures are dominant in the street canyon. The time scale of pollutant concentration variation further increases around the bottom corners, indicating that quite isolated and slower circulations dominate there. The spanwise-averaged multiresolution cospectra demonstrate that the time scale of vertical turbulent transport of pollutants increases from the canyon-top shear layer to the pedestrian-level positions. Interestingly, short and long time-scale transports occur together at the two bottom-corner positions, illustrating that diverging flows and smaller time-scale turbulence transport pollutants in the opposite directions, downward and upward, respectively. Thus, we may need two different transport modes in explaining pollutant dispersion especially at the pedestrian level.

We have shown how instantaneous flow structures drive pollutant dispersion in the two-dimensional street canyon. Nonetheless, how long flow and scalar structures survive and how they interact with the primary vortex are still not clear. To clarify these, we need a sophisticated method that traces volume trajectories of scalar structures (e.g., low-concentration blobs). Combining a Lagrangian tracking method (Lo and Ngan 2017) and a three-dimensional structure identification method (Park et al. 2018) may help the tracking of the ever-changing but coherent structures more accurately. Then, this may result in better representation of dispersion processes as done for three-dimensional street canyons by Belcher et al. (2015).

**Acknowledgements** The authors are grateful to two anonymous reviewers for providing valuable comments on this study. This work was supported by the Research Institute of Basic Sciences funded by the National Research Foundation of Korea (NRF-2019R1A6A1A10073437), and by the Small Grant for Exploratory Research (SGER) program through the National Research Foundation of Korea (NRF-2018R1D1A1A02086007).

## References

- Arakawa A, Lamb VR (1977) Computational design of the basic dynamical processes of the UCLA general circulation model. *Methods Comput Phys* 17:173–265
- Baik JJ, Kim JJ (1999) A numerical study of flow and pollutant dispersion characteristics in urban street canyons. *J Appl Meteorol* 38(11):1576–1589
- Baik JJ, Kim JJ (2002) On the escape of pollutants from urban street canyons. *Atmos Environ* 36(3):527–536
- Belcher SE (2005) Mixing and transport in urban areas. *Philos Trans R Soc* 363(1837):2947–2968
- Belcher SE, Coceal O, Goulart EV, Rudd AC, Robins AG (2015) Processes controlling atmospheric dispersion through city centres. *J Fluid Mech* 763:51–81
- Britter RE, Hanna SR (2003) Flow and dispersion in urban areas. *Annu Rev Fluid Mech* 35:469–496
- Caton F, Britter R, Dalziel S (2003) Dispersion mechanisms in a street canyon. *Atmos Environ* 37(5):693–702
- Cui Z, Cai X, Baker CJ (2004) Large-eddy simulation of turbulent flow in a street canyon. *Q J R Meteorol Soc* 130(599):1373–1394
- Deardorff JW (1980) Stratocumulus-capped mixed layers derived from a three-dimensional model. *Boundary-Layer Meteorol* 18(4):495–527
- Duan G, Jackson JG, Ngan K (2019) Scalar mixing in an urban canyon. *Environ Fluid Mech* 19(4):911–939
- Eliasson I, Offerle B, Grimmond CSB, Lindqvist S (2006) Wind fields and turbulence statistics in an urban street canyon. *Atmos Environ* 40(1):1–16
- Gentine P, Garelli A, Park SB, Nie J, Torri G, Kuang Z (2016) Role of surface heat fluxes underneath cold pools. *Geophys Res Lett* 43(2):874–883
- Han BS, Baik JJ, Kwak KH, Park SB (2018) Large-eddy simulation of reactive pollutant exchange at the top of a street canyon. *Atmos Environ* 187:381–389
- Howell JF, Mahrt L (1997) Multiresolution flux decomposition. *Boundary-Layer Meteorol* 83(1):117–137
- Kwak KH, Lee SH, Seo JM, Park SB, Baik JJ (2016) Relationship between rooftop and on-road concentrations of traffic-related pollutants in a busy street canyon: ambient wind effects. *Environ Pollut* 208:185–197



- Letzel MO, Krane M, Raasch S (2008) High resolution urban large-eddy simulation studies from street canyon to neighbourhood scale. *Atmos Environ* 42(38):8770–8784
- Lo KW, Ngan K (2017) Characterizing ventilation and exposure in street canyons using Lagrangian particles. *J Appl Meteorol Climatol* 56(5):1177–1194
- Maronga B, Moene AF, van Dinter D, Raasch S, Bosveld FC, Gioli B (2013) Derivation of structure parameters of temperature and humidity in the convective boundary layer from large-eddy simulations and implications for the interpretation of scintillometer observations. *Boundary-Layer Meteorol* 148(1):1–30
- Maronga B, Gryschka M, Heinze R, Hoffmann F, Kanani-Sühring F, Keck M, Ketelsen K, Letzel MO, Sühring M, Raasch S (2015) The Parallelized Large-Eddy Simulation Model (PALM) version 4.0 for atmospheric and oceanic flows: model formulation, recent developments, and future perspectives. *Geosci Model Dev* 8(8):2515–2551
- Maronga B, Banzhaf S, Burmeister C, Esch T, Forkel R, Fröhlich D, Fuka V, Gehrke KF, Geletič J, Giersch S, Gronemeier T, Groß G, Heldens V, Hellsten A, Hoffmann F, Inagaki A, Kadasch E, Kanani-Sühring F, Ketelsen K, Khan BA, Knigge C, Knoop H, Krč P, Kurppa M, Maamari H, Matzarakis A, Mauder M, Pallasch M, Pavlik D, Pfaffert J, Resler J, Rissmann S, Russo E, Salim M, Schrempf M, Schwenkel J, Seckmeyer G, Schubert S, Sühring M, von Tils R, Vollmer L, Ward S, Witha B, Wurps H, Zeidler J, Raasch S (2020) Overview of the PALM model system 6.0. *Geosci Model Dev* 13(3):1335–1372
- Marshall JD, Brauer M, Frank LD (2009) Healthy neighborhoods: walkability and air pollution. *Environ Health Perspect* 117(11):1752–1759
- McWilliams JC (1990) A demonstration of the suppression of turbulent cascades by coherent vortices in two-dimensional turbulence. *Phys Fluids A* 2(4):547–552
- Michioka T, Sato A (2012) Effect of incoming turbulent structure on pollutant removal from two-dimensional street canyon. *Boundary-Layer Meteorol* 145(3):469–484
- Oke TR (1988) Street design and urban canopy layer climate. *Energy Buil* 11(1–3):103–113
- Oke TR, Mills G, Christen A, Voogt JA (2017) *Urban climates*. Cambridge University Press, Cambridge
- Oleson KW, Bonan B, Feddema J, Vertenstein M, Grimmond CSB (2008) An urban parameterization for a global climate model. Part I: formulation and evaluation for two cities. *J Appl Meteorol Climatol* 47(4):1038–1060
- Park SB, Baik JJ, Raasch S, Letzel MO (2012) A large-eddy simulation study of thermal effects on turbulent flow and dispersion in and above a street canyon. *J Appl Meteorol Climatol* 51(5):829–841
- Park SB, Baik JJ, Ryu YH (2013) A large-eddy simulation study of bottom-heating effects on scalar dispersion in and above a cubical building array. *J Appl Meteorol Climatol* 52(8):1738–1752
- Park SB, Baik JJ, Lee SH (2015) Impacts of mesoscale wind on turbulent flow and ventilation in a densely built-up urban area. *J Appl Meteorol Climatol* 54(4):811–824
- Park SB, Böing S, Gentine P (2018) Role of surface friction on shallow nonprecipitating convection. *J Atmos Sci* 75(1):163–178
- Pavageau M, Schatzmann M (1999) Wind tunnel measurements of concentration fluctuations in an urban street canyon. *Atmos Environ* 33(24–25):3961–3971
- Rotach M (1995) Profiles of turbulence statistics in and above an urban street canyon. *Atmos Environ* 29(13):1473–1486
- Ryu YH, Baik JJ, Lee SH (2011) A new single-layer urban canopy model for use in mesoscale atmospheric models. *J Appl Meteorol Climatol* 50(9):1773–1794
- Sini JF, Anquetin S, Mestayer PG (1996) Pollutant dispersion and thermal effects in urban street canyons. *Atmos Environ* 30(15):2659–2677
- Uehara K, Murakami S, Oikawa S, Wakamatsu S (2000) Wind tunnel experiments on how thermal stratification affects flow in and above urban street canyons. *Atmos Environ* 34(10):1553–1562
- Vickers D, Mahrt L (2003) The cospectral gap and turbulent flux calculations. *J Atmos Ocean Tech* 20(5):660–672
- Walton A, Cheng A (2002) Large-eddy simulation of pollution dispersion in an urban street canyon—part II: idealised canyon simulation. *Atmos Environ* 36(22):3615–3627
- Wicker LJ, Skamarock WC (2002) Time-splitting methods for elastic models using forward time schemes. *Mon Weather Rev* 130(8):2088–2097
- Williamson J (1980) Low-storage Runge–Kutta schemes. *J Comput Phys* 35(1):48–56
- Xie ZT, Castro IP (2006) LES and RANS for turbulent flow over arrays of wall-mounted obstacles. *Flow Turbul Combust* 76(3):291–312
- Xie ZT, Castro IP (2009) Large-eddy simulation for flow and dispersion in urban streets. *Atmos Environ* 43(13):2174–2185
- Yaghoobian N, Kleissl J, Paw U KT (2014) An improved three-dimensional simulation of the diurnally varying street-canyon flow. *Boundary-Layer Meteorol* 153(2):251–276

---

Zhong J, Cai XM, Bloss WJ (2015) Modelling the dispersion and transport of reactive pollutants in a deep urban street canyon: using large-eddy simulation. *Environ Pollut* 200:42–52

**Publisher's Note** Springer Nature remains neutral with regard to jurisdictional claims in published maps and institutional affiliations.